Quantized Faraday and Kerr rotation and axion electrodynamics of the surface states of three-dimensional topological insulators

Liang Wu,[1*] M. Salehi,[2] N. Koirala,[3] J. Moon,[3]
S. Oh,[3] N. P. Armitage,[1*]

[1]The Institute for Quantum Matter, Department of Physics and Astronomy,
The Johns Hopkins University, Baltimore, MD 21218 USA.
[2]Department of Material Science and Engineering,
Rutgers the State University of New Jersey. Piscataway, NJ 08854
[3]Department of Physics and Astronomy,
Rutgers the State University of New Jersey. Piscataway, NJ 08854

*To whom correspondence should be addressed; E-mail: liangwu.jhu@gmail.com; npa@jhu.edu

June 2, 2022

Topological insulators have been proposed to be best characterized as bulk magnetoelectric materials which show response functions quantized in terms of fundamental physical constants. It has been predicted that this manifests as Faraday and Kerr rotations that are quantized in units of the fine structure constant $\alpha = e^2/2\epsilon_0 hc$. In this work we use a charge-transfer-doping preparation to lower the chemical potential of Bi_2Se_3 films into the bulk gap and as low as $\sim$ 30 meV above the Dirac point, and then probe their low-energy electrodynamic response with high-precision time-domain terahertz polarimetry. As a function of field, a crossover from semi-classical cyclotron resonance to

a quantum regime was observed. In this regime, although the DC transport is still semi-classical, we find quantized Faraday and Kerr rotations the size of which is set by the fine structure constant, which provides evidence for the long-sought axion electrodynamics and the topological magnetoelectric effect of the topological insulator's surface states. Among other aspects, the unique time structure used in such measurements allow us a direct measure of the fine structure constant based on a topological invariant of a solid-state system for the first time.

Topological phenomena in condensed matter physics provide some of the most precise measurements of fundamental physical constants. The measurement of the quantum conductance $G_0 = e^2/h$ from the quantum Hall effect (*1*) and the flux quantum $\Phi_0 = h/2e$ from the Josephson effect (*2, 3*) provide the most precise value for Planck's constant h. In the last number of years a new class of materials in the form of topological insulators has been discovered (*4–6*). These are materials in which topological properties of the bulk wavefuctions give rise to a topologically protected surface metal with a novel massless Dirac spectrum. It has been proposed that topological insulators are best characterized not as *surface* conductors, but as *bulk* magnetoelectrics (*7, 8*) with a quantized magnetoelectric response coefficient whose size is set by the fine structure constant $\alpha = e^2/2\epsilon_0 hc$. Such a topological measurement could provide precise values for three fundamental physical constants: the electric charge e, Planck's constant h, and the speed of light c in a solid-state context.

Magnetoelectrics are materials in which a polarization can be created by an applied magnetic field or a magnetization can be created by an applied electric field and have been topics of interest for decades (*9*). Representative examples of magnetoelectric (ME) materials are Cr_2O_3 (*10*) with an $\mathbf{E}\cdot\mathbf{B}$ ME coupling of the form proposed by Dzyaloshinskii and multiferroic $BiFeO_3$ (*11*) with an $\mathbf{E}\times\mathbf{B}$ ME coupling. Topological insulators can be characterized as special $\mathbf{E}\cdot\mathbf{B}$

magnetoelectrics (*7, 8*), which in the topological field theory can be shown to be a consequence of an additional term $\mathcal{L}_\theta = -2\alpha\sqrt{\frac{\epsilon_0}{\mu_0}}\frac{\theta}{2\pi}\mathbf{E}\cdot\mathbf{B}$ added to the usual Maxwell Lagrangian (*7*). Here α is the fine structure constant, and ϵ_0 and μ_0 are the permittivity and permeability of free space. It was shown that if time-reversal symmetry (TRS) is preserved then three-dimensional insulators can be divided into two classes of materials, in which the θ term in $\mathcal{L}_\theta$ is either $2\pi(N+\frac{1}{2})$ (topological) or $2\pi(N)$ (conventional band insulators) (*7*). Here N is an integer that indicates the highest fully filled Landau level (LL) of the surface when TRS is broken weakly. θ can be formulated as a bulk quantity modulo a quantum (here 2π) in much the same way as the electric polarization **P** in a ferroelectric can only be defined as a bulk quantity moduluo a dipole quantum that depends on the surface charge (*12*). An analogy can be made between the physics described here to that of the hypothetical axion particle that was proposed to explain charge conjugation parity symmetry violation (CP violation) in the strong interaction by Wilczek (*13*) and hence a topological magnetoelectric effect (TME) of this kind has been called axion electrodynamics. The axion has not been observed in particle physics experiments, but one may study the analogs effect in the context of topological insulators.

In the limit where a TRS breaking field is finite, but vanishingly small at the surface, and the surface chemical potential is tuned to the Dirac point a modified Maxwell's equations can be derived (see supplementary information (SI) section **1**) from the full Langragian. The modified Gauss's and Ampère's laws read

$$\nabla\cdot\mathbf{E} = \frac{\rho}{\epsilon_0} - 2c\alpha\nabla(\frac{\theta}{2\pi})\cdot\mathbf{B}. \tag{1}$$

$$\nabla\times\mathbf{B} = \mu_0\mathbf{J} + \frac{1}{c^2}\frac{\partial\mathbf{E}}{\partial t} + \frac{2\alpha}{c}[\mathbf{B}\frac{\partial}{\partial t}(\frac{\theta}{2\pi}) + \nabla(\frac{\theta}{2\pi})\times\mathbf{E}]. \tag{2}$$

The consequences of axion electrodynamics and the TME are the additional source and current terms related to the derivatives of θ in these modified Maxwell's equations. The additional

source term leads to an effect whereby an electric charge placed near the surface of a TI creates an image magnetic monopole (*14*). The additional current term gives a novel half-integer quantum Hall effect (QHE) on the TI surface (*7*). Although there has been indirect evidence for half-integer QHE effects in gated TI $BiSbTeSe_2$ exfoliated flakes (*15*), gated $(Bi_{1-x}Sb_x)_2Te_3$ thin films (*16*) and surface charge-transfer doped pure Bi_2Se_3 films (*17*) at very high magnetic fields, it is generally not straightforward to observe the QHE in a conventional transport style experiment as one does with a 2D electron gas (2DEG) with leads connected to sample edges as TIs have a closed surface with no boundaries. It is desirable then to use non-contact probes such as Faraday and Kerr rotations (*7, 18, 19*), which have been predicted to be quantized in the units of the fine structure constant α. One can proceed from the modified Ampère's law Eq. 20 in conjunction with the usual Faraday's law to derive the reflection and transmission coefficients for a traveling wave incident on a TI surface (See SI section **2**). In an applied magnetic field, one finds that for a TI thin film on a simple dielectric substrate, the Faraday rotation in the quantum regime is

$$\tan(\phi_F) = \frac{2\alpha}{1+n}(N_t + \frac{1}{2} + N_b + \frac{1}{2}), \tag{3}$$

where $n \sim 3.1$ is the THz range index of refraction of the sapphire and N_t, N_b are the highest fully filled LL of the top and bottom surfaces, which depend on the chemical potential and size of the TRS breaking field. Note that unlike the typical case of a magnetoelectric which must break both TRS and inversion symmetry, a TI in magnetic field breaks only TRS. This means that the magnetoelectric effect can be considered as such only locally for a particular surface as the surface trivially breaks inversion. The net effect of considering a local TRS breaking field that is oppositely directed for the two surfaces in our thin film geometry gives Eq. 25.

There have been a number of inter-related challenges in realizing the TME on both the materials and instrumentation side. First, one must have a negligible level of bulk carriers and a

low chemical potential at the surface, but most known topological insulators suffer from inadvertent bulk doping. A metallic gate used to gate away charge carriers in transport experiments cannot be used in an optical experiment because it would have its own Faraday effect. Second, as the topological field theory is derived for the translationally invariant case, one may expect that it will only apply when the TRS breaking perturbation is strong enough to overcome disorder and establish a surface quantum Hall effect. Third, to reveal the TME it is required that the probe frequencies and temperatures be well below the effective cyclotron frequency of the surface states, which for small fields is $\omega_c = \frac{e|\mathbf{B}|\mathbf{v}_F}{\hbar \mathbf{k}_F}$ (where $\mathbf{v}_F$ is the Fermi velocity and $\mathbf{k}_F$ is the Fermi wave vector). In practice this put the relevant frequency in the sub-THz part of the electromagnetic spectrum, which has been a traditionally difficult frequency range to characterize materials in. Fourth, THz range experiments with their long wavelengths require large uniform samples of at least a few mm in spatial extent. Fifth, as the size of the effect is set by the fine structure constant, the expected rotations are expected to be very small and well beyond the capacity of conventional THz range polarimetry.

Despite these challenges, due to a number of innovations, we have succeeded in measuring the quantized TME effect using time-domain THz spectroscopy (TDTS) (1 THz $\sim$ 4.14 meV), using recently developed low-density and high-mobility Bi_2Se_3 molecular beam epitaxy films, in conjunction with a novel high-precision polarimetry technique (*20*). TDTS is a powerful tool to study the long-wavelength (low-energy) electrodynamics of topological insulators. Samples are thin films of Bi_2Se_3 grown by molecular beam epitaxy with a recently developed recipe that results in true bulk insulating TIs with low surface chemical potential. These films were further treated $in\ situ$ by a thin charge transfer layer of deposited MoO_3 that further decreases the carrier density. MoO_3 is semiconductor with a gap $\sim$ 3 eV (*21*) and does not contribute to Faraday rotation. Details of the film growth can be found in Ref. (*17*).

In Fig. 1(a), we show the real part of the conductance of new generation Bi_2Se_3 films with

and without the MoO_3 layer in zero magnetic field as compared to the conductance of an older (but still excellent (*22, 23*)) generation of Bi_2Se_3 films. As shown in previous work (*22, 23*), the complex conductance can be characterized by a low-frequency Drude term peaked at zero frequency, a phonon term peaked at $\sim$ 1.9 THz and a lattice polarizability contribution ϵ_∞ (See SI section **4** for details). The total area below the Drude conductance is the Drude spectral weight and is a function of the carrier density. One can see that MoO_3 lowers the spectral weight and therefore the carrier density. In previous work (*22, 23*) we have shown that this spectral weight is independent of film thickness establishing a principle surface transport channel. In the present case there is a weak dependence of this spectral weight on thickness below 10 QL as shown in SI section **4**. We believe this is because for this generation of samples, the substantial dopants come from bulk defects (as opposed to surface defects in earlier generation samples) that move to the surface and work as surface carriers. Additionally it is likely that MoO_3 is more effective in reducing carrier density in thinner samples.

As a part of the magneto-THz experiments described below, we measure the low field cyclotron resonance frequency and find the effective mass (See SI section **3** for raw data). As show in Fig. 1(b), a decreased effective mass from 0.15 m_e to 0.07 m_e is observed through charge transfer to MoO_3, which is consistent with the known band structure for Dirac surface states. Both bulk states or a trivial 2DEG from an accumulation layer will exhibit a carrier-density independent mass. Moreover 0.07 m_e is lower than any reported bulk or 2DEG effective mass. Converting the spectral weight or effective mass to chemical potential using the known band structure of Bi_2Se_3 these new films with MoO_3 have E_F of 30 - 60 meV above the Dirac point and in the bulk gap when an equal contribution from the two surface states is assumed (See SI section **1**). Below, we focus only on the thin films treated with MoO_3.

Having identified the topological surface states and verified the low Fermi energy of these films, we explore their low-frequency Faraday rotation. The experimental configuration is

shown in Fig. 2(a). We measure complex Faraday rotation through TDTS with the polarization modulation technique (*20, 24*). The Faraday rotation is a complex quantity in which the real part is the rotation of the major axis of the ellipse and the imaginary part is related to the ellipticity as shown in Fig. 2(b). The full-field data of a 10 QL sample is shown in Fig. 2(c) (d). At low fields ($<$ 4 T), the Faraday rotation shows semi-classical cyclotron resonance, as demonstrated by the shifting of the inflection point (close to the zero value) in the real part and the shifting of the minimum in the imaginary part with fields as discussed in Ref. (*24*). Typical cyclotron frequency is marked by red arrows for data at 2.5 T for instance. For the 10 QL sample, above 5 T, the inflection point in the real part of the Faraday rotation moves above our high frequency range and the low-frequency tails becomes flat and overlaps even higher field data. In our TDTS measurements, top and bottom states are measured simultaneously and so the quantized Faraday rotation is given by Eq. 25.

Since the resolution of our THz polarimetry is within 1 mrad, we conclude that 10 QL sample enters the quantized regime when field is above 5.75 T with its low-frequency tails falling on the expectation for the $5\frac{2\alpha}{1+n}$ plateau. Similarly, as shown in Fig. 2(e) 6 QL, 8 QL, 12 QL and 16 QL, the low-frequency Faraday rotations falls on the $2\frac{2\alpha}{1+n}$, $4\frac{2\alpha}{1+n}$, $7\frac{2\alpha}{1+n}$ and $7\frac{2\alpha}{1+n}$ plateaus respectively. Aside from the filling factor differences, the only qualitative differences between samples is that thicker samples have a narrower magnetic field range where the Faraday rotation is quantized because they have a slightly higher carrier density and filling factor at the same magnetic fields (See SI section **4**).

In our experiment, we measure the top and bottom surfaces of the thin film simultaneously. Essential for our interpretation in terms of the TME is that we can treat the top and bottom surfaces independently. Previous ARPES work (*25*) showed that the hybridization gap from top and bottom surfaces was an exponential function of thickness for film thicknesses less than 6 QL. Extrapolating this data to thicker films (as done in Ref. (*26*)) gives a hybridization gap Δ

of 1 meV at 10 QL. Treating the hybridization between top and bottom surfaces as a simple two level system (and assuming a strictly linear massless Dirac spectrum) with degenerate Dirac points on top and bottom surfaces, shows that the mixing between top and bottom surfaces will be of order $\Delta/4E_F$. For our 10 QL sample this is approximately 0.005 which should be considered negligible. 12 QL and 16 QL samples have even smaller hybridization gaps predicted of 0.3 meV and 0.01 meV respectively and hence have even less overlap of the surface states. Note that theoretical calculations of finite-size effects in Bi_2Se_3 give a systematically even smaller Δ at a given thickness, which if realized would even further suppress any mixing of top and bottom surfaces (*27*).

We can contrast our experiments with DC transport that have shown quantized Hall resistivity plateaus in these films only above $\sim$ 24 T as shown for a typical sample 8 QL film in Fig. 2(f). When an external magnetic field is applied perpendicular to the films, top and bottom surface states are gapped due to LL formation while the side surfaces parallel to the magnetic field remain still gapless because a small in-plane magnetic field can be treated as a shift of the Dirac points (*28*). As the quantized Hall resistance in a usual transport measurement on a 2DEG arise from ballistic transport in 1D edge channels when leads are attached, one must go to very high magnetic fields for a TI in order to not have the non-chiral side states contributes (*17*). In the present case, THz radiation is focused onto a local spot far from the edges of the film so they do not contribute to the spectral response.

Data in Fig. 2 gives evidence for a Faraday rotation set by the fine structure constant. However, such measurements by themselves are limited, as Eq. 25 shows that the Faraday rotation still depends non-universally on the index of refraction of the substrate. Our ability to measure the fine structure constant to high precision is limited by our knowledge of n. However, by using the explicit time structure of TDTS we can define and measure a quantity that depends only on the fine structure constant (and surface filling factors). When THz light is transmitted

through a film and substrate, the substrate itself can be used as an optical resonator (*22, 29*) resulting in a series of pulses that each have different histories of interaction with the film as shown in Fig. 3(a). The 1st peak that is transmitted through the film undergoes a Faraday rotation, whereas the 2nd peak undergoes an additional reflection and Kerr rotation ϕ_K. By subtracting the Faraday rotation, we can measure the Kerr rotation separately. In the quantized regime, one can show (see SI) that the Kerr rotation (to factors up to second order in α) is

$$\tan(\phi_K) = \frac{4n\alpha}{n^2-1}(N_t + \frac{1}{2} + N_b + \frac{1}{2}). \tag{4}$$

A representative 10 QL sample for the Kerr rotation is shown in Fig. 3(c)(d). Similar to the Faraday rotation, the signatures of cyclotron resonances are inflection points in the real part and dips in the imaginary part. Above 5.75 T, the Kerr rotation of a 10 QL sample is quantized as $5\frac{4n\alpha}{n^2-1}$ to within our experimental resolution at frequencies below 0.8 THz. The prefactor of 5 is the same as arrived at in the Faraday rotation. We measured Kerr rotation on samples with different thickness, 6 QL, 8 QL, 12 QL and 16 QL and in all cases the rotation is accurately given by $\frac{4n\alpha}{n^2-1}$ times the filling factor found in the Faraday rotation experiments as shown in Fig. 3(e). Eqs. 25 and 27 show that combining Faraday and Kerr rotation in a single measurement allows one to eliminate the dependence on the index of substrate and to measure the fine structure constant directly. One finds that

$$\alpha_{measured} = \frac{1}{N_t + N_b + 1/2 + 1/2} \frac{\tan(\phi_F)^2 - \tan(\phi_F)\tan(\phi_K)}{\tan(\phi_K) - 2\tan(\phi_F)}. \tag{5}$$

Measuring these quantities in a single scan and taking ratios in this fashion also serves to minimize the systematic noise in the output for $\alpha_{measured}$. Using $N_t + N_b + 1/2 + 1/2 = 5$ and 7 for the 10 QL and 12 QL samples respectively, we plot the results of Eq. 29 for two samples in Fig. 4 and find for both the measured value is close to 1/137 ($\sim$ 7.3) mrad. Averaging over the frequency range that quantized rotation is observed ($<$ 0.8 THz) for all

samples measured, we find a best measured value for α_{meas} of 1/137.9, which is close to the accepted value 1/137.04. This is the first direct measurement of the finite structure constant based on a topological invariant (and in a purely solid state context). Although the level of precision we have achieved for α is far less than for instance its determination via the anomalous magnetic moment of the electron (*30*), the quantization should be considered quite good. Its deviation from the accepted value is approximately 0.5%, which can be compared favorably to the quantization seen in the quantum spin Hall effect which was only quantized to the 10% level (*31*). If this measurement could be further refined it could, along with measures of the Josephson effect and quantized Hall resistances in 2DEGs provide a purely solid state measure in a redefined conventional electrical unit scheme for the impedance of free space $Z_0 = \sqrt{\mu_0/\epsilon_0}$. Currently, both μ_0 and ϵ_0 are defined quantities in the International System of Units. With μ_0 staying a defined quantity (and essential for the definition of the Ampere), a measure of α would allow c to become a measured quantity in a condensed matter experiment.

With advances in high-quality Bi_2Se_3 films and charge-transfer doping by MoO_3 to lower the chemical potential to as low as ~ 30 meV above the Dirac point coupled to the development of high-precision time-domain THz polarimetry, we have observed quantized Faraday rotation and Kerr rotation from topological surface states. The quantized responses we find here should not be viewed as a simple manifestation of the quantized quantum Hall transport seen in usual 2DEGs, since TI surface states live on a closed 2D manifold embedded in 3D space. For instance, our DC transport does not show a quantized Hall resistance in this field range. In a formalism where the TIs are described as bulk magnetoelectrics, this response can be described in the context of a topological magnetoelectric effect and axion electrodynamics. Among other things, this provides a direct solid-state measure of the fine structure constant. The observation of this effect gives a definitive characterization of topologically insulating states of matter. It may prove to be an essential tool in the discovery of theoretically anticipated states of matter

such as fractional topological insulators in the form of a fractional magnetoelectric effect (*32*).

We thank M. Franz, T. Hughes, A. MacDonald, J. Moore, M. Orlita, V. Oganesyan, W.-K. Tse, A. Turner, R. Valdés Aguilar, X. L. Qi and S.C. Zhang for helpful discussions. THz experiments were supported by the Army Research Office Grant W911NF-15-1-0560 with additional support by the Gordon and Betty Moore Foundation through Grant GBMF2628 to NPA at JHU. Film growth for this work was supported by the NSF DMR-1308142, EFMA-1542798 and the Gordon and Betty Moore Foundation EPiQS Initiative Grant GBMF4418 to SO at Rutgers.

References and Notes

1. K. v. Klitzing, G. Dorda, M. Pepper, *Phys. Rev. Lett.* **45**, 494 (1980).

2. B. D. Josephson, *Physics letters* **1**, 251 (1962).

3. P. W. Anderson, J. M. Rowell, *Physical Review Letters* **10**, 230 (1963).

4. J. E. Moore, *Nature* **464**, 194 (2010).

5. M. Z. Hasan, C. L. Kane, *Rev. Mod. Phys.* **82**, 3045 (2010).

6. X.-L. Qi, S.-C. Zhang, *Rev. Mod. Phys.* **83**, 1057 (2011).

7. X.-L. Qi, T. L. Hughes, S.-C. Zhang, *Phys. Rev. B* **78**, 195424 (2008).

8. A. M. Essin, J. E. Moore, D. Vanderbilt, *Phys. Rev. Lett.* **102**, 146805 (2009).

9. M. Fiebig, *Journal of Physics D: Applied Physics* **38**, R123 (2005).

10. I. Dzyaloshinskii, *Soviet Physics Jetp-Ussr* **10**, 628 (1959).

11. J. Wang, *et al.*, *Science* **299**, 1719 (2003).

12. D. Vanderbilt, R. D. King-Smith, *Phys. Rev. B* **48**, 4442 (1993).

13. F. Wilczek, *Phys. Rev. Lett.* **58**, 1799 (1987).

14. X.-L. Qi, R. Li, J. Zang, S.-C. Zhang, *Science* **323**, 1184 (2009).

15. Y. Xu, *et al.*, *Nature Physics* **10**, 956 (2014).

16. R. Yoshimi, *et al.*, *Nature Communications* **6** (2015).

17. N. Koirala, *et al.*, *Nano Letters* **15**, 8245 (2015).

18. J. Maciejko, X.-L. Qi, H. D. Drew, S.-C. Zhang, *Phys. Rev. Lett.* **105**, 166803 (2010).

19. W.-K. Tse, A. H. MacDonald, *Phys. Rev. Lett.* **105**, 057401 (2010).

20. C. Morris, R. Valdés Aguilar, A. Stier, N. P. Armitage, *Optics Express* **20**, 12303 (2012).

21. Z. Hussain, *Journal of Materials Research* **16**, 2695 (2001).

22. R. Valdés Aguilar, *et al.*, *Phys. Rev. Lett.* **108**, 087403 (2012).

23. L. Wu, *et al.*, *Nature Physics* **9**, 410 (2013).

24. L. Wu, *et al.*, *Physical Review Letters* **115**, 217602 (2015).

25. Y. Zhang, *et al.*, *Nature Physics* **6**, 584 (2010).

26. D. Kim, P. Syers, N. P. Butch, J. Paglione, M. S. Fuhrer, *Nature Communications* **4** (2013).

27. J. Linder, T. Yokoyama, A. Sudbø, *Physical review B* **80**, 205401 (2009).

28. S. S. Pershoguba, V. M. Yakovenko, *Physical Review B* **86**, 165404 (2012).

29. J. N. Hancock, *et al.*, *Phys. Rev. Lett.* **107**, 136803 (2011).

30. P. J. Mohr, B. N. Taylor, *Reviews of modern physics* **72**, 351 (2000).

31. M. König, *et al.*, *Science* **318**, 766 (2007).

32. B. Swingle, M. Barkeshli, J. McGreevy, T. Senthil, *Phys. Rev. B* **83**, 195139 (2011).

33. M. Peskin, D. Schroeder, *An introduction to quantum field theory* (1995).

34. N. P. Armitage, *Physical Review B* **90**, 035135 (2014).

35. M. Salehi, *et al.*, *APL Materials* **3**, 091101 (2015).

36. M. T. Edmonds, *et al.*, *ACS nano* **8**, 6400 (2014).

37. U. Fano, *Physical Review* **124**, 1866 (1961).

38. H. Beidenkopf, *et al.*, *Nat. Phys.* **7**, 939 (2011).

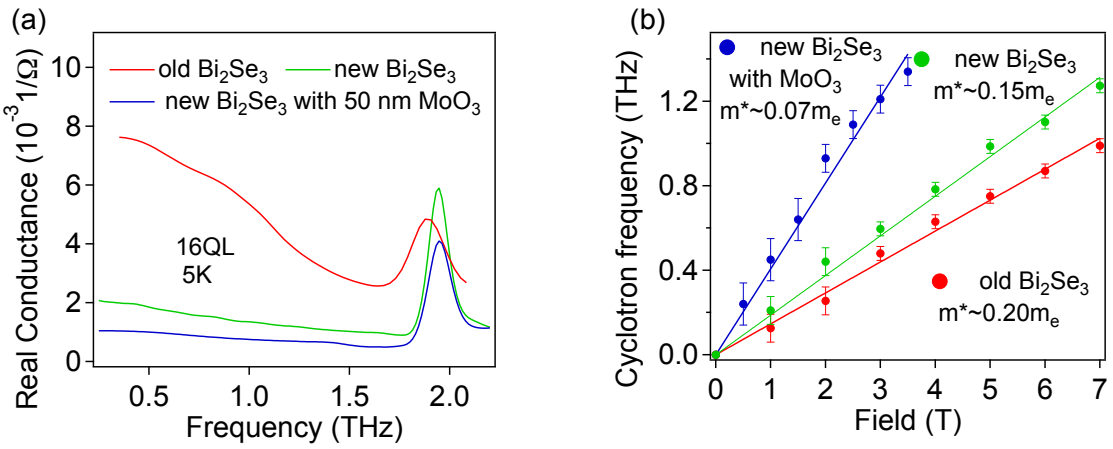

Figure 1: (Color online) (a) Zero-field real conductance (b) Cyclotron frequencies ($\omega_c/2\pi$) vs. field of 16 QL old Bi_2Se_3, new Bi_2Se_3 and new Bi_2Se_3 with MoO_3 at 5 K. The solid lines in (b) are linear fits that give the effective mass from $\frac{\omega_c}{2\pi} = \frac{eB}{m^*}$ in the low field classical cyclotron resonance regime.

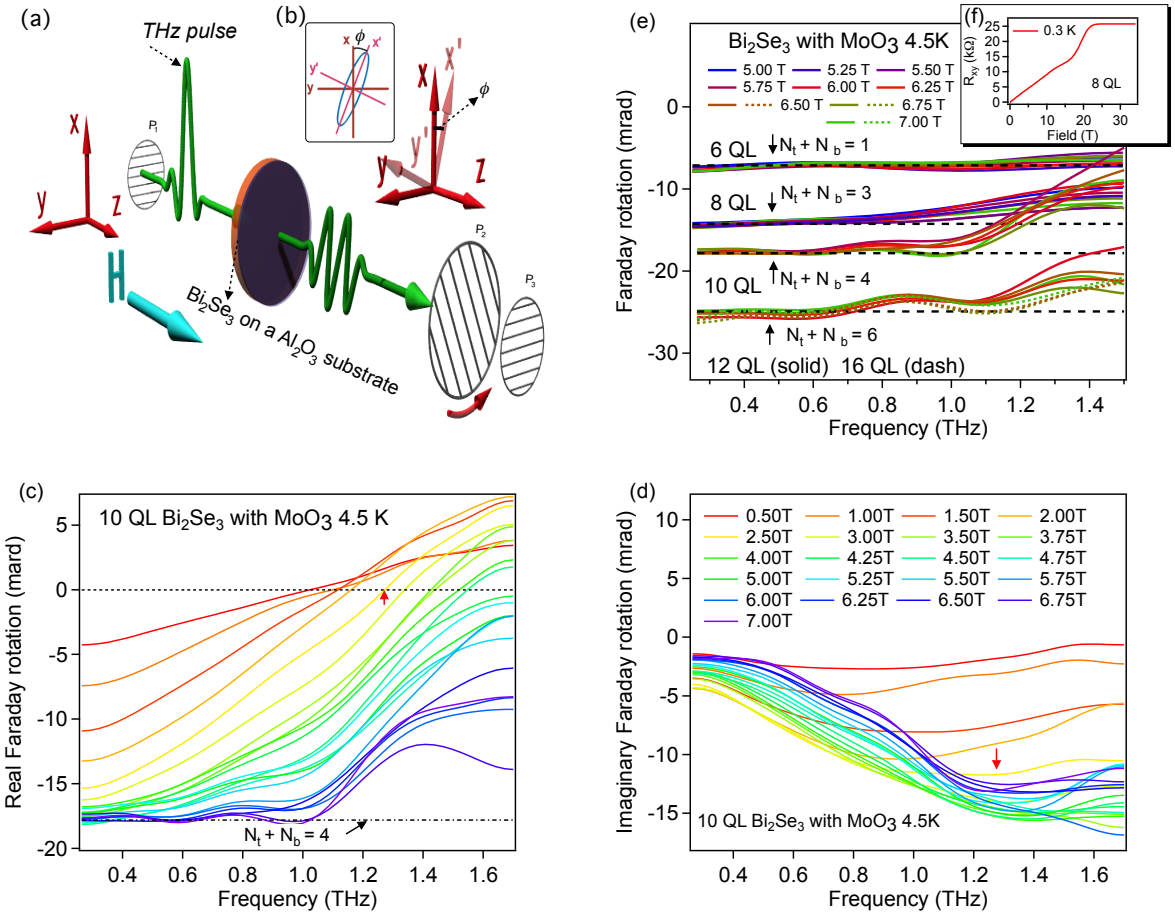

Figure 2: (Color online) (a) Schematic diagram of the Faraday rotation experiment. P_1, P_2 and P_3 are polarizers. The polarization plane (xz) of the linearly polarized incoming THz beam is rotated by the Faraday angle ϕ_F (into the $x'z$ plane) after passing through Bi_2Se_3 on a sapphire substrate in a perpendicular magnetic field (z direction). The polarization acquires an ellipticity simultaneously, as shown in (b). (c) Real part of Faraday rotation of 10 QL new Bi_2Se_3 with MoO_3 at 4.5 K. Dashed line is the expectation from Eq. 25. (d) Imaginary part of Faraday rotation. (e) Quantized Faraday rotation for different samples. Dashed lines are theoretical expectation values assuming certain values for the filling factor of the surface states. (f) DC transport Hall resistance of a representative 8 QL sample.

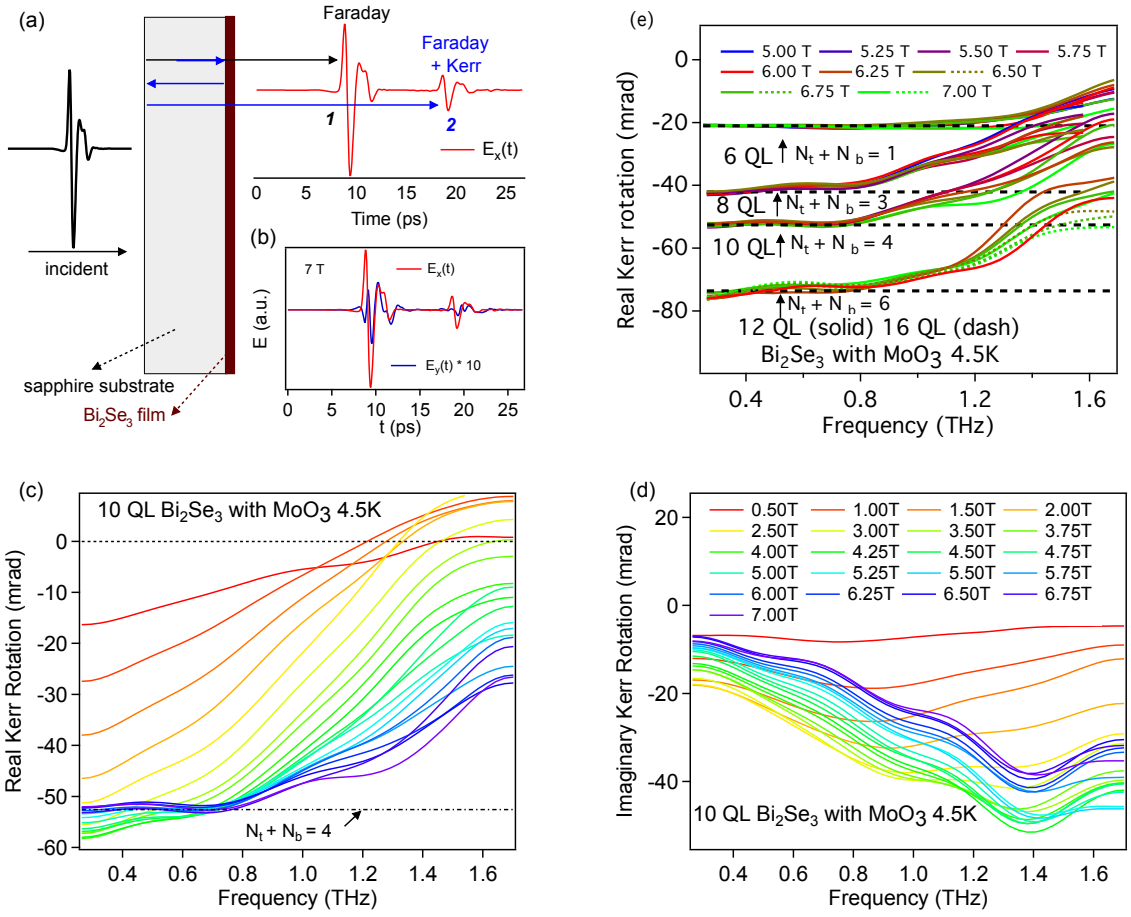

Figure 3: (Color online) (a) Schematic diagram of the Kerr rotation experiment. The black and blue arrows shows the optical path for the 1st and 2nd pulses in the time trace. (b) $E_x(t)$ and $E_y(t)$ time traces of 10 QL new Bi_2Se3 with MoO_3 at 4.5 K. (c) Real (d) Imaginary part of Kerr rotation of 10 QL new Bi_2Se3 with MoO_3 at 4.5 K. (e) Quantized Kerr rotation for different samples.

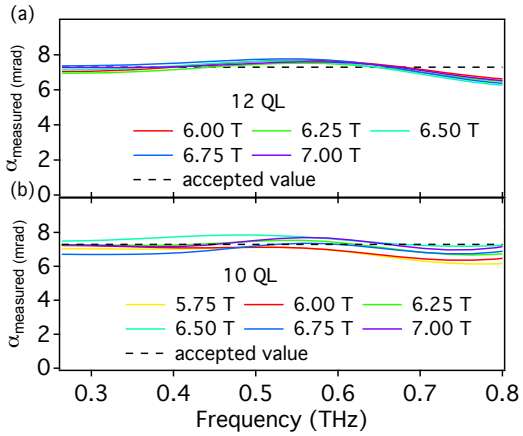

Figure 4: (Color online) The measured fine structure constant of (a) 12 QL (b) 10 QL new Bi_2Se_3 with MoO_3 at different field at 4.5 K.

Supplementary Information for "Quantized Faraday and Kerr rotation and axion electrodynamics of the surface states of three-dimensional topological insulators"

1 Derivation of Modified Maxwell's Equations

Qi et al. (*7*) showed that the electrodynamics of topological insulators can be described by adding an additional topological term $\mathcal{L}_\theta$ to the usual Maxwell Lagrangian $\mathcal{L}_0$. Here we rederive the modified Maxwell's equations in the conventional 3D vector component notation, which will be more familiar to many readers of this section as compared to the relativistic Einstein notation that is typical in the field theory literature. The two terms in the Lagrangian density written down in potential form are

$$\mathcal{L}_0 = \frac{\epsilon_0}{2}(\nabla\phi + \frac{\partial \mathbf{A}}{\partial t})^2 - \frac{1}{2\mu_0}(\nabla \times \mathbf{A})^2 - \rho\phi + \mathbf{J}\cdot\mathbf{A}, \tag{6}$$

$$\mathcal{L}_\theta = -2\alpha\sqrt{\frac{\epsilon_0}{\mu_0}}\frac{\theta}{2\pi}(\nabla\phi + \frac{\partial \mathbf{A}}{\partial t})\cdot(\nabla \times \mathbf{A}). \tag{7}$$

Here α is the fine structure constant and ϵ_0 and μ_0 are the permittivity and permeability of the free space. The topological contribution θ is an angle $2\pi(N + \frac{1}{2})$ where N is an integer that indicates the highest fully filled Landau level (LL) of the surface when TRS is broken weakly. It can be formulated as a bulk quantity only modulo a quantum (here 2π) in much the same way as the electric polarization **P** in a ferroelectric can only be defined as a bulk quantity modulo a dipole quantum that depends on the surface charge (*8, 12*). The action is

$$\mathcal{S} = \mathcal{S}_0 + \mathcal{S}_\theta = \int dt\, d^3x\, (\mathcal{L}_0 + \mathcal{L}_\theta) \tag{8}$$

where $\mathcal{S}_\theta$ derives from the additional term and $\mathcal{S}_0$ is the usual Maxwell action. One can start with

with Eq. 8 and perform the typical variation of the potentials in the action to get modifications to Gauss's law and Ampère's law. The Gauss's law term comes from variations in the scalar potential ϕ. One defines

$$\delta\mathcal{S} = \mathcal{S}(\phi) + \mathcal{S}(\phi + \delta\phi) = \delta\mathcal{S}_0 + \delta\mathcal{S}_\theta \tag{9}$$

where $\delta\phi$ is an infinitesimal. As found in standard references (*33*) the Maxwell part of the variation is

$$\delta\mathcal{S}_0 = -\int dt\, d^3x\, [\epsilon_0 \nabla \cdot (\nabla\phi + \frac{\partial \mathbf{A}}{\partial t}) + \rho]\delta\phi. \tag{10}$$

For the new term to first order in $\delta\phi$ one has a variation

$$\delta\mathcal{S}_\theta = \int dt\, d^3x\, [-2\alpha\sqrt{\frac{\epsilon_0}{\mu_0}}\frac{\theta}{2\pi}(\nabla \times \mathbf{A}) \cdot \nabla\delta\phi]. \tag{11}$$

As with the Maxwell term, one shifts the derivatives to the other spatially dependent terms in the integrand by integration by parts. The surface terms can be set to zero. One has

$$\delta\mathcal{S}_\theta = \int dt\, d^3x\, \nabla \cdot [2\alpha\sqrt{\frac{\epsilon_0}{\mu_0}}\frac{\theta}{2\pi}(\nabla \times \mathbf{A})]\delta\phi. \tag{12}$$

Expanding the divergence and using the fact that the divergence of curl is zero one has

$$\delta\mathcal{S}_\theta = \int dt\, d^3x\, [\nabla(\frac{\theta}{2\pi}) \cdot 2\alpha\sqrt{\frac{\epsilon_0}{\mu_0}}(\nabla \times \mathbf{A})]\delta\phi. \tag{13}$$

We add this to the variation of the usual Maxwell action to get

$$\delta\mathcal{S} = \int dt\, d^3x\, [-(\epsilon_0 \nabla \cdot (\nabla\phi + \frac{\partial \mathbf{A}}{\partial t}) + \rho) + 2\alpha\sqrt{\frac{\epsilon_0}{\mu_0}}\nabla(\frac{\theta}{2\pi}) \cdot (\nabla \times \mathbf{A})]\delta\phi. \tag{14}$$

Setting the variation of the total action to zero requires the term in the brackets above be equal to zero. Rearranging and substituting back in for the fields, one gets a modified version of Gauss's law that reads

$$\nabla \cdot \mathbf{E} = \frac{\rho}{\epsilon_0} - 2c\alpha\nabla(\frac{\theta}{2\pi}) \cdot \mathbf{B}. \tag{15}$$

To get the modified version of Faraday's law one must vary the vector potential. Expanding $\mathcal{S}(\mathbf{A} + \delta\mathbf{A})$ to first order in $\delta\mathbf{A}$ one has for the Maxwell term

$$\delta\mathcal{S}_0 = \int dt\, d^3x\, [-\epsilon_0 \frac{\partial(\nabla\phi + \partial\mathbf{A}/\partial t)}{\partial t} - \nabla \times (\nabla \times \mathbf{A})/\mu_0 + \mathbf{J}] \cdot \delta\mathbf{A} \tag{16}$$

For $\mathcal{S}_\theta$ we have

$$\delta\mathcal{S}_\theta = \int dt\, d^3x\, [-2\alpha\sqrt{\frac{\epsilon_0}{\mu_0}}\frac{\theta}{2\pi}(\frac{\partial\delta\mathbf{A}}{\partial t} \cdot (\nabla \times \mathbf{A}) + (\nabla\phi + \frac{\delta\mathbf{A}}{\delta t}) \cdot (\nabla \times \delta\mathbf{A}))] \tag{17}$$

Now we integrate by parts by moving the derivative with respect to time on the first term and the gradient on the second. Setting the surface terms to zero and after some simplification one gets

$$\delta\mathcal{S}_\theta = \int dt\, d^3x\, [2\alpha\sqrt{\frac{\epsilon_0}{\mu_0}}(\frac{\partial\theta/\partial t}{2\pi}(\nabla \times \mathbf{A}) - \nabla(\frac{\theta}{2\pi}) \times (\nabla\phi + \frac{\partial\mathbf{A}}{\partial t})] \cdot \delta\mathbf{A}. \tag{18}$$

The total variation then reads

$$\delta\mathcal{S} = \int dt d^3x [-\epsilon_0 \frac{\partial(\nabla\phi + \partial\mathbf{A}/\partial t)}{\partial t} - \nabla\times(\nabla\times\mathbf{A})/\mu_0 + \mathbf{J} + 2\alpha\sqrt{\frac{\epsilon_0}{\mu_0}}(\frac{\partial\theta/\partial t}{2\pi}(\nabla\times\mathbf{A}) - \nabla(\frac{\theta}{2\pi})\times(\nabla\phi + \frac{\partial\mathbf{A}}{\partial t}))] \cdot \delta\mathbf{A}. \tag{19}$$

As before if the total variation is to be zero for any infinitesimal $\delta\mathbf{A}$ then the quantity in brackets must be zero. Rearranging and again substituting in for the fields, one finds a modified version of Ampère's law that reads

$$\nabla \times \mathbf{B} = \mu_0 \mathbf{J} + \frac{1}{c^2}\frac{\partial \mathbf{E}}{\partial t} + \frac{2\alpha}{c}[\mathbf{B}\frac{\partial}{\partial t}(\frac{\theta}{2\pi}) + \nabla(\frac{\theta}{2\pi}) \times \mathbf{E}]. \tag{20}$$

2 Derivation of Modified Fresnel and Transmission Equations

One can use the modified Ampère's law Eq. 20 with usual Faraday's law to derive to find modified boundary conditions for the electric and magnetic field and from there reflection and transmission coefficients for a traveling wave. A non-topological surface current $\mathbf{J}$ could be included in this derivation, but we neglect it here because the chemical potential of our samples are in the gap. One can show for instance that the modified inverse transmission matrix for transmission across the vacuum-TI interface is

$$\hat{T}^{-1} = \begin{bmatrix} \frac{1}{2}(1+c/v) & \frac{2\alpha\theta}{2\pi} \\ -\frac{2\alpha\theta}{2\pi} & \frac{1}{2}(1+c/v) \end{bmatrix}, \tag{21}$$

where v is the speed of light inside the TI. For a slab system with broken TRS, the transmission is most easily computed with circular eigenstates (*34*). For incoming light polarized polarized along the x direction, for an isotropic sample the Faraday rotation is given by

$$\tan(\phi_F) = \mathrm{T}_{xy}/\mathrm{T}_{xx} = \frac{1}{i}\frac{\mathrm{T}_{++} - \mathrm{T}_{--}}{\mathrm{T}_{++} + \mathrm{T}_{--}}, \tag{22}$$

where for instance T_{xx} and T_{xy} are diagonal and off-diagonal terms in the Jones transmission matrix (not to be confused with the Fresnel transmission coefficient for light across an interface given by the inverse of Eq. 21) in the xy coordinate frame and T_{++} and T_{--} are diagonal terms in the transmission matrix for the circular basis. (See Ref. (*34*) for details about the various bases of Jones matrices and their introconversions). In the limit where the thickness of the film is much less than the wavelength of the incident light, the effect of the two conducting surfaces

can be treated as single surface with effective conductance $G^{\text{eff}} = G_t + G_b$. The transmission then of a thin film on a substrate with index of refraction n referenced to a nominally identical substrate is

$$\mathrm{T}_{++} = \frac{1+n}{1+n+Z_0 G^{\text{eff}}_{++}}, \tag{23}$$

were $Z_0 = \sqrt{\frac{\mu_0}{\epsilon_0}}$ is the impedance of free space. Small differences in substrate thickness ΔL from the reference can be easily dealt with by multiplying by a phase factor $e^{i\omega\Delta L(n-1)/c}$. Eq. 23 applied to Eq. 22 yields

$$\tan(\phi_F) = \frac{Z_0 G^{\text{eff}}_{xy}}{2+2n+Z_0 G^{\text{eff}}_{xx}}, \tag{24}$$

in the quantum regime for the TIs $G^{\text{eff}}_{xx} \to 0$ and $G^{\text{eff}}_{xy} = \frac{e^2}{h}(N_t + \frac{1}{2} + N_b + \frac{1}{2})$ and

$$\tan(\phi_F) = \frac{2\alpha}{1+n}(N_t + \frac{1}{2} + N_b + \frac{1}{2}), \tag{25}$$

used in the main text follows. The expression for $\tan(\phi_K)$ derived in the main text can be derived in a similar fashion.

$$\tan\phi_K = \frac{2Z_0 n G^{eff}_{xy}}{n^2 - [1 + 2Z_0 G^{\text{eff}}_{xx} + Z_0^2(G^{\text{eff}2}_{xx} + G^{\text{eff}2}_{xy})]}. \tag{26}$$

In the quantum regime,

$$\tan(\phi_K) = \frac{4n\alpha}{n^2-1}(N_t + \frac{1}{2} + N_b + \frac{1}{2}). \tag{27}$$

Note that this expression neglects a correction coming from the $G^{\text{eff}2}_{xy}$ in the denominator of Eq. 26, that to lowest order goes as α^3. This correction is completely undetectable at the current level of precision of the experiment, but may be important formally. If we consider the correction of α^3,

$$\tan(\phi_K) = \frac{4n\alpha}{n^2 - 1 - 4\alpha^2}(N_t + \frac{1}{2} + N_b + \frac{1}{2}). \tag{28}$$

we can still write down a universal expression of the fine structure constant in terms of Faraday rotation and Kerr rotation as following and define the topological invariant.

$$\alpha_{measured} = \frac{1}{N_t + N_b + 1/2 + 1/2} \frac{\tan(\phi_F)^2 - \tan(\phi_F)\tan(\phi_K)}{\tan(\phi_K) - 2\tan(\phi_F) - \tan(\phi_F)^2\tan(\phi_K)}. \tag{29}$$

Due to the small size of the rotations, the third term in the denominator makes a negligible contribution to the fine structure constant we measure and so we have neglected it in the main text.

3 Experimental methods

Thin films of Bi_2Se_3 were grown at Rutgers University by molecular beam epitaxy (MBE) on an insulating $Bi_{2-x}In_xSe_3$ buffer layer on top of 0.5 mm thick crystalline Al_2O_3 substrates. Films grow a quintuple layer (1 unit cell) at a time (1 QL $\sim$1 nm). 50 nm MoO_3 was deposited in-situ and was followed by 100 nm amorphous Se to reduce aging effects (*35*). Details on the growth can be found elsewhere (*17*). Films grow a quintuple layer (1 unit cell) at a time (1 QL$\sim$1 nm).

Time-domain THz spectroscopy (TDTS) in a transmission geometry was performed with a home-built spectrometer. An approximately single-cycle picosecond pulse of light is transmitted through the sample and the substrate. One measures electric field in a phase-sensitive TDTS measurement. The complex transmission is obtained from the ratio of a Fourier transform of a sample scan over a Fourier transform of a substrate scan. The complex conductance can be directly inverted from the transmission equation in the thin film limit without using Kramers-Kronig transformation (*23*):

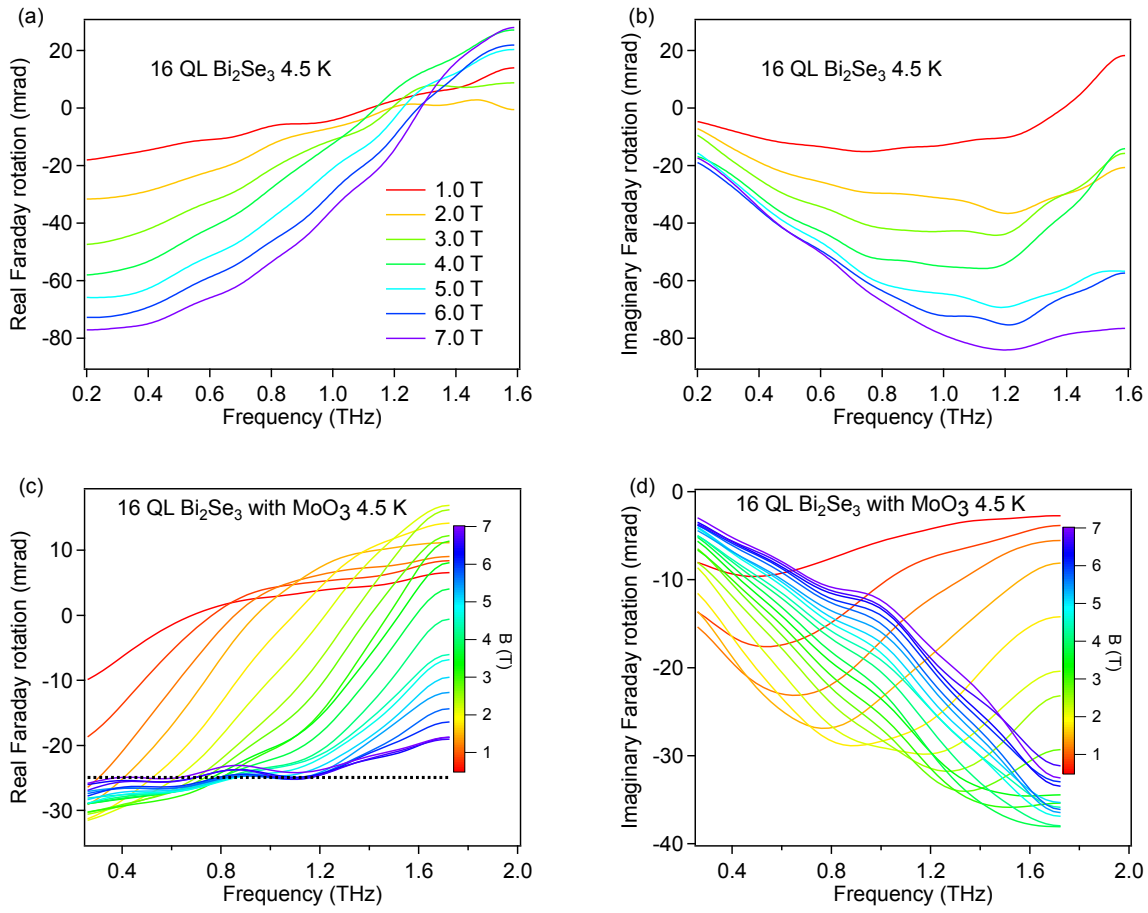

Figure 5: (a) Real part and (b) Imaginary part of the complex Faraday rotation of a bare 16 QL Bi_2Se_3 sample at different fields with a 1 T step at 4.5 K. (c) Real part and (d) Imaginary part of the complex Faraday rotation of a 16 QL Bi_2Se_3/MoO_3 sample at different fields at 4.5 K. We used 0.50 T step below 3.50 T and 0.25 T step above 3.50 T.

$$\tilde{T}(\omega) = \frac{1+n}{1+n+Z_0 G(\omega)} e^{i\omega(n-1)\Delta L/c} \tag{30}$$

where ΔL is the small difference in thickness between the sample and reference substrates, n is the real index of refraction of substrate and Z_0 is the vacuum impedance.

Complex Faraday and Kerr rotation measurements were performed in a closed-cycle 7 T superconducting magnet at low temperature. We use the polarization modulation technique to measure the rotation and ellipticity accurately and the experimental details were discussed in early works (*20, 24*).

4 Terahertz data and discussions

The conductance and cyclotron frequencies vs. field of a 16 QL Bi_2Se_3 and a 16 QL Bi_2Se_3/MoO_3 is shown in Fig. 1 in the main text. Here we show the complex Faraday rotation of these two samples in Fig. 5 in the SI. We can see that the surface treatment of MoO_3 with its charge-transfer mechanism (*36*) reduces the Faraday rotation by almost a factor of 4. This is consistent with the depletion of the surface charge carriers. One can also find that the cyclotron frequencies (inflection points in the real part and dip positions in the imaginary part) of MoO_3-treated samples are much lower and the features are more pronounced because the in-situ MoO_3 capped sample has a higher mobility ($\sim$ 3500 $cm^2/V{\cdot}s$) (*17*) than a bare Bi_2Se_3 sample ($\sim$ 1400 $cm^2/V{\cdot}s$) (*35*) after an overnight shipping in a vacuum bag.

The zero-field complex conductance of 16 QL, 12 QL, 10 QL, 8 QL and 6 QL Bi_2Se_3/MoO_3 samples at 5K is shown in Fig. 6. As done in previous work (*24*), we used a Drude-term, a phonon term and a lattice polarizability ϵ_∞ term to model the data.

$$G(\omega) = \epsilon_0 d \left(-\frac{\omega_{pD}^2}{i\omega - \Gamma_D} - \frac{i\omega\omega_{pDL}^2}{\omega_{DL}^2 - \omega^2 - i\omega\Gamma_{DL}} - i\left(\epsilon_\infty - 1\right)\omega \right) \tag{31}$$

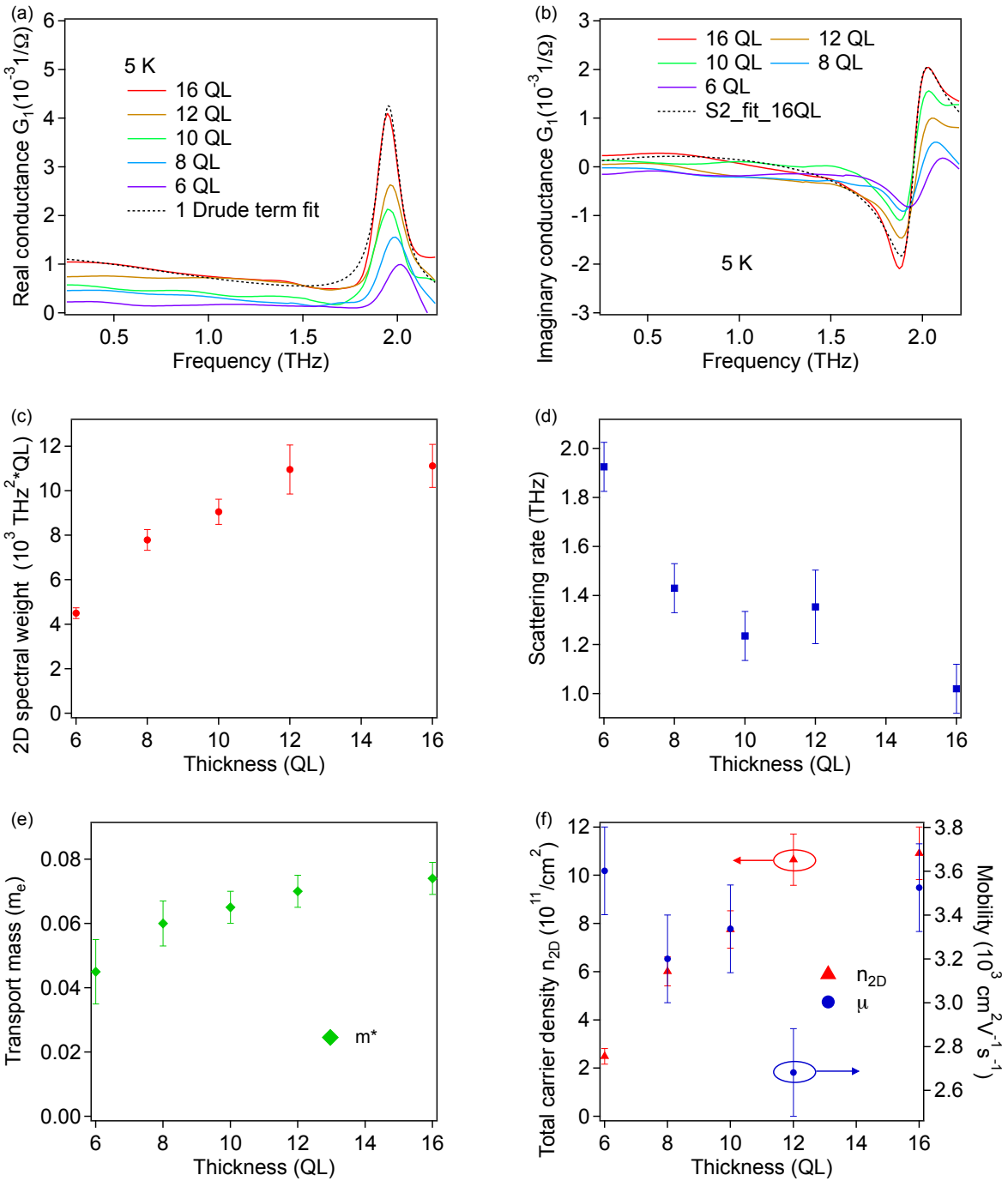

Figure 6: (a) Real part and (b) Imaginary part of complex conductance of 16 QL, 12 QL, 10 QL, 8 QL and 6 QL Bi_2Se_3/MoO_3 samples at 5K. (c) Spectral weight and (d) Scattering rate of the Drude term vs thickness. (e) Measured cyclotron mass VS thickness. (f) Extracted total sheet carrier density (red) and mobility (blue) vs thickness.

Here we focus on the Drude term which is related to the surface carrier dynamics. The spectral weight ($\omega_{pD}^2 d$) is proportional to the integrated area of the real part of the Drude conductance. It gives the ratio of carrier density to an effective transport mass.

$$\frac{2}{\pi\epsilon_0}\int G_{D1}d\omega = \omega_{pD}^2 d = \frac{n_{2D}e^2}{m^*\epsilon_0} \tag{32}$$

The scattering rate Γ_D is half-maximum width of the Drude term peaked at zero frequency. The fit quality containing one Drude term is showed in Fig. 6(a) (b). The overall fit is excellent except for the asymmetry near the phonon frequency that is believe to be due to a Fano interaction (*37*). It is not considered in the Drude-Lorentz analysis here because it does not affect the low-frequency Faraday and Kerr rotation.

The Drude-Lorentz model does not give carrier density directly. In order to extract the information about carrier density and mobility, one need to measure the cyclotron mass. We consider the conductance in the semi-classical regime by including a cyclotron frequency ω_c term in the circular base and model the complex Faraday rotation.

$$G_\pm = -i\epsilon_0\omega d\left(\frac{\omega_{pD}^2}{-\omega^2 - i\Gamma_D\omega \mp \omega_c\omega} + \frac{\omega_{pDL}^2}{\omega_{DL}^2 - \omega^2 - i\omega\Gamma_{DL}} + (\epsilon_\infty - 1)\right) \tag{33}$$

Details can be found in a previous work (*24*). We consider one Drude term first. By extracting the cyclotron frequency in the semi-classical regime and using a linear fit $\frac{\omega_c}{2\pi} = \frac{eB}{m^*}$, one can measure the cyclotron mass m*, as shown in Fig.6 (e). Using the surface state dispersion up to a quadratic correction fit from ARPES data ($E = Ak_F + Bk_F^2$) and $m^* = \hbar k_F/v_F$, one can estimate the chemical potential of these samples are 30 meV, 45 meV, 50 meV, 60 meV and 60 meV with $\sim$5 meV uncertainty for 6 QL, 8 QL, 10 QL, 12 QL and 16 QL respectively.

We also performed fits by treating the top and bottom independently and did a two-Drude component fit for the Faraday rotation (fit results not shown). We found that in such low-density samples, the difference of cyclotron masses of top and bottom surfaces is not more than 0.01

~ 0.01 m_e. Note that in such low-carrier-density samples, the fluctuation of the chemical potential in real space is also important. Scanning tunneling microscopy (STM) shows that Dirac point energy distribution in real space has a Gaussian width 20 - 40 meV (*38*). Considering the chemical potential fluctuation in a typical topological insulators sample is very close to the average chemical potential of the samples studied here, treating top and bottom surface approximately the same in the classical regime is a good approximation. At low fields (below 3.5 T), the Landau Level (LL) filling factors may differ a little in real space, the transition between Landau Levels may overlap with each other, which results in a classical cyclotron resonance in the spectra. In other words, the cyclotron mass we extracted from the one-Drude component fit is an average mass of two surface states. However, when the samples reach the quantum regime, small difference in chemical potential may show up in spectrum such as 6 QL and 8 QL.

Going back to Fig. 6, we discuss the semi-classical regime only. When cyclotron mass (an average mass) is measured, one can estimate the total sheet carrier density by using $\omega_{pD}^2 d = \frac{n_{2D}e^2}{m^*\epsilon_0}$ and average mobility by using $\mu = e/\Gamma_D m^*$. The extracted carrier density and mobility are shown in Fig. 6 (f), the values of which agree with the low-field DC transport (*17*).

In the first generation of experiments using THz on the residual bulk-conducting Bi_2Se_3 samples, a thickness-independent spectral weight was interpreted as an evidence for surface state transport (*22, 23*), which was further verified by a topological phase transition experiments (*23*) and, more directly, by measuring the cyclotron mass of this channel (*24*). Note that in these Bi_2Se_3 grown on sapphire directly, the total carrier density is $\sim 3 \times 10^{13}$ /cm^2. Even though chemical potential may differ by ~ 40 meV for different samples which was observed in Ref. (*24*), it only change the chemical potential by ~ 10 $\%$ because the surface state Fermi energy is ~ 350 meV. Spectral weight will not show a noticeable change in these high-carrier-density films when the chemical potential changes by 40 meV.

However, in the current generation of low-carrier-density Bi_2Se_3 samples grown on an in-

sulating $Bi_{2-x}In_xSe_3$ buffer layer, the total carrier density is $\sim$ 1 - 3 $\times$ 10^{12} /cm^2 (*17*). Carrier density changes from sample to sample (*17*), which will show up as an observable change in the spectral weight if the chemical potential differs by 40 meV. Also, when the thickness is lower than 16 QL, the carrier density decreases (*17*). When these samples were further treated with MoO_3 through a charge transfer process, the carrier density is further lowered to $\sim$ 2 - 8 $\times$ 10^{11} /cm^2 below 10 QL, sample variation and thickness-dependent carrier density are expected in such a low-density regime. For instance, we also measured another 16 QL Bi_2Se_3/MoO3 and found that Faraday rotation quantized at $N_t + N_b = 5$ (data not show). We have also found that MoO_3 is not effective in depleting carrier in thicker films (for example 32 QL). This indicates that MoO_3 is less effective in depleting the carrier on the bottom surface in thicker samples. In thinner samples, either because the top and bottom surfaces are connected by side surface states or through a tunneling process, MoO_3 is very effective in reducing the total carrier density. We believe a thickness-dependent spectral weight (or carrier density) is not surprising in these samples with ultra-low carrier densities.